# Gyrokinetic Analyses of Core Heat Transport in JT-60U Plasmas with Different Toroidal Rotation Direction

Emi NARITA, Mitsuru HONDA[1)], Nobuhiko HAYASHI[1)], Hajime URANO[1)], Shunsuke IDE[1)] and Takeshi FUKUDA

*Graduate School of Engineering, Osaka University, Suita, Osaka 565-0871, Japan*

*[1)]Japan Atomic Energy Agency, Naka, Ibaraki 311-0193, Japan*

(Received 18 December 2014 / Accepted 11 February 2015)

Tokamak plasmas with an internal transport barrier (ITB) are capable of maintaining improved confinement performance. The ITBs formed in plasmas with the weak magnetic shear and the weak radial electric field shear are often observed to be modest. In these ITB plasmas, it has been found that the electron temperature ITB is steeper when toroidal rotation is in a co-direction with respect to the plasma current than when toroidal rotation is in a counter-direction. To clarify the relationship between the direction of toroidal rotation and heat transport in the ITB region, we examine dominant instabilities using the flux-tube gyrokinetic code GS2. The linear calculations show a difference in the real frequencies; the counter-rotation case has a more trapped electron mode than the co-rotation case. In addition, the nonlinear calculations show that with this difference, the ratio of the electron heat diffusivity $\chi_e$ to the ion's $\chi_i$ is higher for the counter-rotation case than for the co-rotation case. The difference in $\chi_e/\chi_i$ agrees with the experiment. We also find that the effect of the difference in the flow shear between the two cases due to the toroidal rotation direction on the linear growth rate is not significant.



Keywords: heat transport, toroidal rotation, flux-tube gyrokinetic code

DOI: 10.1585/pfr.10.1403019

## 1. Introduction

Improved confinement tokamak plasmas are often associated with an internal transport barrier (ITB). The heat diffusivity $\chi$ is reduced in the ITB region, which leads to an improvement in the energy confinement [1]. Improvement of the energy confinement is a key to forming and maintaining a high normalized beta $\beta_N$ plasma [2]. Exploring the steady-state operation scenarios in the high $\beta_N$ domain is one of the objectives of JT-60SA and ITER [3, 4]. Therefore understanding the mechanism of ITB formation is a key step towards realizing this objective. There are a number of ITB types, and one is the "parabolic type" ITB [5]. In plasmas with parabolic type ITB, the pressure increases smoothly starting from the ITB foot towards the magnetic axis [5]. The parabolic type ITB is observed in both reversed magnetic shear plasmas and weak magnetic shear plasmas [1]. Another type of ITB is the "box type" ITB. Plasmas with this ITB type only have the steep pressure gradient within the ITB layer, and the pressure profile is relatively flat in the inner and outer regions separated by this layer. The box type ITB has been observed only in reversed magnetic shear plasmas [1]. In JT-60U, the roles of toroidal rotation in weak magnetic shear plasmas with parabolic type ITB were studied using neutral beam (NB) injection, and it was found that toroidal rotation in a co-direction with respect to the plasma current yields a steeper gradient of the electron temperature, $T_e$-ITB, than that provided by toroidal rotation in the counter-direction [2]. Both plasmas have a weak shear in the radial electric field $E_r$. It has also been reported that in plasmas with the box type ITB, the $E_r$ shear is strong enough to suppress turbulence in the ITB layer [1, 6]. Parabolic type ITB discharges do not have the strong $E_r$ shear characteristic of box type ITB discharges. On the other hand, conventional H-mode plasmas have the positive magnetic shear and the weak $E_r$ shear in the core region, although these plasmas do not have an ITB. In the plasmas, improved confinement has been determined to be due to the increased pedestal temperature associated with co-toroidal rotation and profile resilience in the core region [7]. From these comparisons, the difference in the $T_e$-ITB between parabolic type ITB plasmas with different rotation directions may not be significantly related to the $E_r$ shear. To clarify the relationship between the direction of toroidal rotation and heat transport in the ITB region, we examined the dominant instabilities using the flux-tube gyrokinetic code GS2 [8, 9].

The GS2 code is a nonlinear initial-value code, which solves gyrokinetic equations for the perturbed distribution function $\delta f$ in the frame rotating with toroidal rotation, where the distribution function $f$ is split into an equilibrium part $F$ and a perturbed part $\delta f$ [10]. We use GS2 to examine the dominant instabilities, including the effects of collisionality, kinetic-electrons, finite-$\beta$, plasma shaping

author's e-mail: narita.emi@eb.see.eng.osaka-u.ac.jp

via actual equilibria, etc. Recently, a toroidal flow shear effect has been implemented and studied in some gyrokinetic codes. These studies demonstrate turbulent transport with the flow shear (see e.g., Refs. [10–13]). In GS2, two effects of the rotational shear are implemented: transport suppression due to the $\boldsymbol{E}\times\boldsymbol{B}$ velocity shear and transport enhancement due to the parallel velocity gradient (PVG) [10, 11]. In this paper, we investigate plasmas with different rotation profiles, thereby examining the flow shear effects on instabilities.

The rest of this paper is organized as follows. Sec. 2 outlines the main points of the experiments. We also present transport simulations using the transport model GLF23 [14,15], which can calculate dominant instabilities. In addition, since GLF23 is the most widely used transport model, we also check the reproducibility of the differences in the $T_e$-ITB. In Sec. 3, the linear instabilities in the co- and counter-rotating plasmas are investigated using GS2 without the flow shear effect. These linear calculations explain the dominant instabilities in more detail than the transport simulations using GLF23. In order to compare the linear results with the experimental results, we estimate the ratio of the electron heat diffusivity $\chi_e$ to the ion's $\chi_i$ by the nonlinear calculations. Since the ratio, $\chi_e/\chi_i$, can change as the dominant instabilities change, we confirm whether or not $\chi_e^{\rm nonlin}/\chi_i^{\rm nonlin}$ calculated by the nonlinear simulations shows the similar tendency with respect to the instabilities predicted by the linear calculations, and then $\chi_e^{\rm nonlin}/\chi_i^{\rm nonlin}$ is compared to the experiment. In Sec. 4, we examine the effects of the flow shear on linear growth rates to investigate how the flow shear affects the linear calculations. Finally, we present our conclusions and discussion in Sec. 5.

# 2. Overview of Experiment

## 2.1 Main points of experiment

The high confinement performance of long-pulse ELMy H-mode plasmas with parabolic type ITBs was established in JT-60U [2]. These plasmas have both high $\beta_N$ and high thermal confinement enhancement factor $H_{\rm H98(y,2)}$. In Ref. [2], the role of plasma rotation on the quality of the ITB was examined by switching the NB injection from a co- to counter-injection during a discharge. It has been reported that as a consequence, improvement of the $T_e$-ITB performance was observed with co-rotating plasmas. The temporal evolution of the injected NB power $P_{\rm NB}$, the toroidal rotation velocity $V_T$, the ion temperature $T_i$, and the electron temperature $T_e$ are shown in Fig. 1. $V_T$ and $T_i$ are measured with charge exchange recombination spectroscopy, and $T_e$ is measured by Thomson scattering. Experimental profiles of the co- ($t$ = 9.0 s) and counter-rotating ($t$ = 15.0 s) plasmas are shown in Fig. 2: the toroidal magnetic field $B_T$ = 1.6 T, the plasma current $I_p$ = 0.9 MA, the on-axis electron density $n_{e0} \sim 3\times10^{19}$ m$^{-3}$, the on-axis ion and electron temperatures $T_{i0} \sim 7$ (6) keV

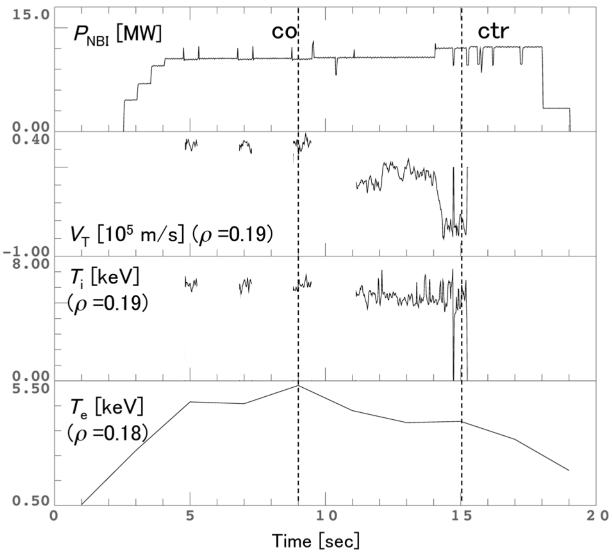


Fig. 1 Waveforms of the injected NB power $P_{\rm NB}$, the toroidal rotation velocity $V_T$, the ion temperature $T_i$, and the electron temperature $T_e$ in JT-60U discharge 46861.

and $T_{e0} \sim 6$ (4) keV, respectively, for the co- (counter-) rotation case, and the safety factor at the 95% flux surface $q_{95} \sim 3$. Since the electron density $n_e$ is almost equivalent for the two cases as shown in Fig. 2(a), we focus on the effects of temperature gradient and the flow shear on the heat transport. The effective ion charge $Z_{\rm eff}$ is assumed to have a constant radial profile of $Z_{\rm eff}$ = 3 (3.5) for the co- (counter-) rotation case. Therefore, despite the virtually identical $n_e$, there are differences in the main ion and impurity densities between the two cases. The safety factor $q$ (Fig. 2(b)) is almost identical for the two cases. As shown in Fig. 2(c), these plasmas have different toroidal rotation profiles. Figure 2(d) shows the $E_r$ profiles calculated by the 1.5D integrated code TOPICS [16]. In TOPICS, $E_r$ is determined by the radial force balance equation with the neoclassical parallel momentum balance equation [17]. The $E_r$ profiles do not have steep gradients in the core region in either case; a notched $E_r$ structure is not observed, which is a characteristic in the box type ITB discharges. As shown in Fig. 2(e), the $T_i$ profile is influenced by the direction of toroidal rotation only in the pedestal region, and the gradients are almost equivalent in the core region. This way of making changes in a profile with toroidal rotation is similar to that for conventional H-mode plasmas described in Sec. 1. The $\chi_i$ profiles shown in Fig. 2(g) for the two cases are similar to each other. The $T_e$ profiles of both cases have an ITB, and the ITB foot is around $\rho \sim 0.6$, where the $T_e$ gradients start to increase toward the magnetic axis (Fig. 2(f)). Here $\rho$ is the normalized minor radius defined by the toroidal flux. Outside of the ITB foot, $\rho \gtrsim 0.6$, the two $T_e$ profiles are almost identical. However, a difference in $T_e$ is observed for $\rho \lesssim 0.45$, and the gradient for the co-rotation case is steeper than that for the counter-rotation

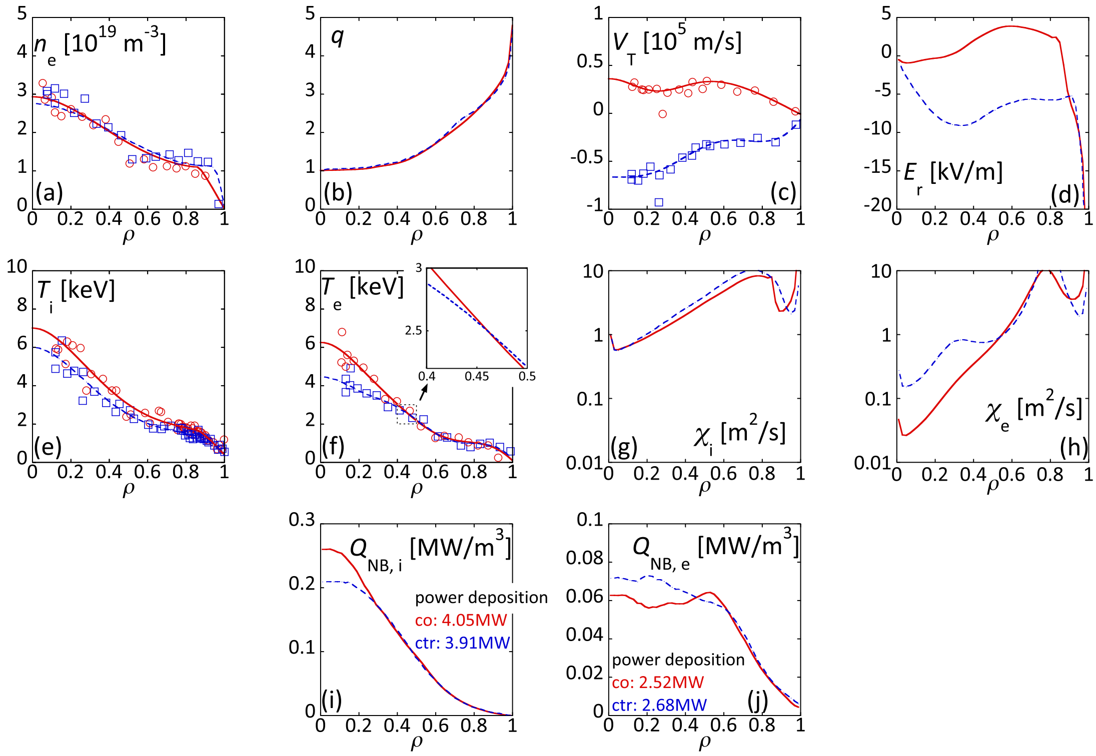


Fig. 2 Experimental profiles for JT-60U discharge 46861 in the co-rotating phase, $t$ = 9.0 s, (solid lines) and the counter-rotating phase, $t$ = 15.0 s, (dashed lines): (a) the electron density $n_e$, (b) the safety factor $q$, (c) the toroidal rotation velocity $V_T$, (d) the radial electric field $E_r$, the temperatures of (e) ions $T_i$ and (f) electrons $T_e$ and a closeup (the upper right figure), the heat diffusivities of (g) ions $\chi_i$ and (h) electrons $\chi_e$ and the deposition power of the injected NB for (i) ions $Q_{NB,i}$ and (j) electrons $Q_{NB,e}$.

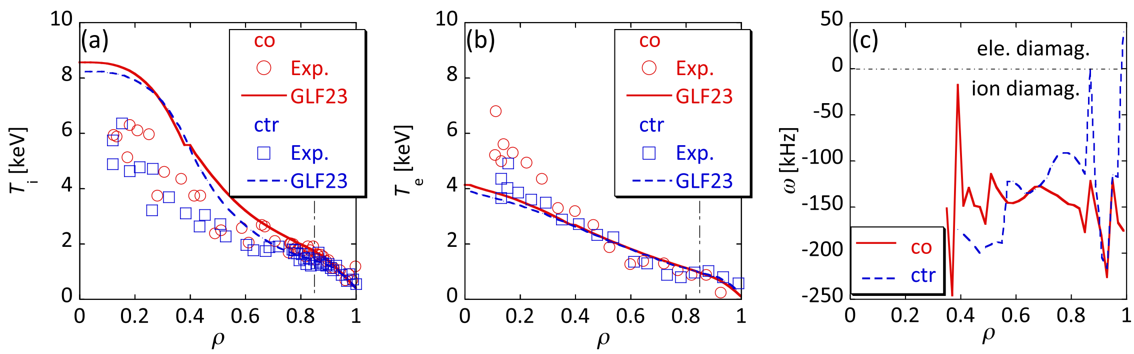


Fig. 3 Simulation results with GLF23 for the co-rotation case (solid lines) and the counter-rotation case (dashed lines). Predicted (a) ion and (b) electron temperatures with experimental values for the co-rotation case (circles) and for the counter-rotation case (squares). The temperatures are calculated inside $\rho$ = 0.85, as denoted by the vertical chain lines. (c) Predicted real frequency of the fastest growing mode in low wavenumbers for the ITG/TEM modes.

case in the ITB region, $\rho \lesssim 0.6$. The difference in $\chi_e$ is also clearly observed in Fig. 2(h). During this discharge, the power deposition profile is maintained as much as possible (Figs. 2(i) and 2(j)). Therefore, the difference in the $T_e$-ITB is not due to the heating power.

## 2.2 Analyses with transport model GLF23

We performed heat transport simulations to predict temperature profiles using the transport model GLF23 [14, 15], which is a widely used model based on drift wave turbulence. In this section, we investigate the dominant instabilities in the plasmas and check the reproducibility of the differences in the $T_e$-ITB. In this model, a mixing length formula is used to obtain the value of $\chi$ with 10 wavenumbers for the ion temperature gradient (ITG) mode and the trapped electron mode (TEM) and 10 wavenumbers for the electron temperature gradient (ETG) mode. GLF23 includes the effect of $E_r$ via the $\boldsymbol{E} \times \boldsymbol{B}$ shearing rate, which stabilizes the ITG/TEM modes. The $\boldsymbol{E} \times \boldsymbol{B}$ shearing rate is defined as $\gamma_{E\times B} \equiv \frac{\rho}{q}\frac{\partial}{\partial\rho}(-\frac{\partial\phi}{\partial\psi})$, where $q$, $\phi$,

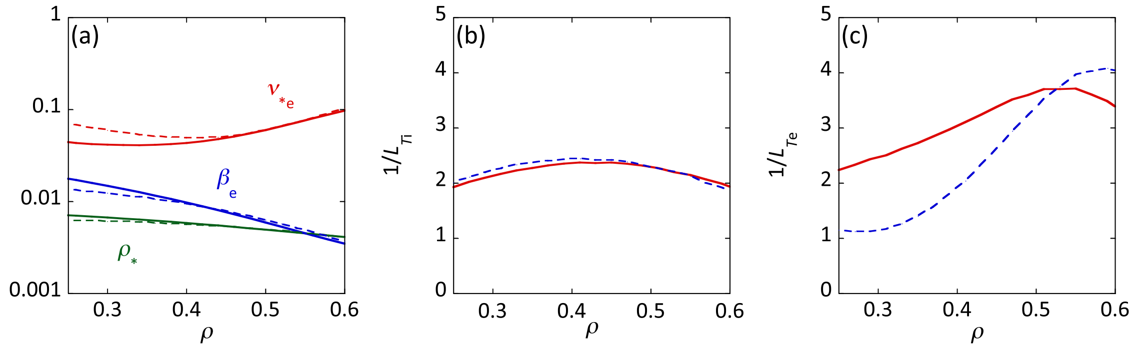


Fig. 4 Transport-relevant profiles for the co-rotation (solid lines) and the counter-rotation (dashed lines) cases: (a) the electron collisionality $\nu_{*e}$, the electron beta $\beta_e$ and the normalized Larmor radius $\rho_*$, (b) normalized ion temperature gradients $1/L_{T_i}$, and (c) normalized electron temperature gradients $1/L_{T_e}$.

and $\psi$ are the safety factor, the electrostatic potential, and the poloidal flux function, respectively. We use GLF23 by implementing it in the 1.5D integrated code TOPICS [16]. In these simulations, ion and electron temperatures are calculated for $\rho < 0.85$. The neoclassical and anomalous heat diffusivities are given by the Matrix Inversion (MI) method [18] and GLF23, respectively. Profiles of the density and pedestal temperatures are fixed to the experimental ones, and the MHD equilibrium is also fixed. Figures 3(a) and 3(b) show the results of the calculations. The value of $T_i$ is similarly overestimated for both the co- and counter-rotation cases. On the other hand, the predicted $T_e$ is similar to the experimental $T_e$ outside of the ITB foot. However, in the ITB region, the predicted $T_e$ profiles for the two cases are comparable, and the difference in the gradient between the two cases observed in the experiment is not reproduced by GLF23. Figure 3(c) shows the real frequency $\omega$ of the fastest growing mode in low wavenumbers for the ITG/TEM modes. The positive (negative) $\omega$ indicates propagation in the electron (ion) diamagnetic direction. Both cases have the ITG instability for $\rho \gtrsim 0.3$. For $\rho \lesssim 0.3$, while the ITG/TEM modes are stable, the ETG mode drives electron heat transport in the calculations. It has been reported that GLF23 tends to underestimate the $T_e$ profile due to the transport coefficient, as driven by the ETG mode being overestimated [15]. This would explain why the predicted $T_e$ is lower than the experimental value.

## 3. Analyses with GS2 Code without Flow Shear

To examine the dominant instabilities in the ITB regions of the co- and counter-rotating plasmas in more detail than the transport simulation using GLF23, we perform linear calculations with the GS2 code [8, 9]. These calculations use MHD equilibria in G EQDSK format taken from the JT-60U database and include electron collisions and electromagnetic effects. The calculations employ three gyrokinetic species: main ions (deuterons), electrons, and a single impurity species (carbon). The fast ions are assumed to be the main ions. Figure 4(a) shows profiles of the electron collisionality $\nu_{*e}$, the electron beta $\beta_e$, and the normalized Larmor radius $\rho_*$ defined as $\rho_* = \rho_i/a$, where $\rho_i = c_s M/(eB)$ with $c_s = (T_e/M)^{0.5}$, the deuterium mass $M$, the ion charge $e$, and the magnetic field $B$. At $\rho = 0.45$, where the values of $T_e$ are almost equivalent, the normalized $n_e$, $T_i$, and $T_e$ gradients are $1/L_{n_e} \sim 1.5$, $1/L_{T_i} \sim 2.4$, and $1/L_{T_e} \sim 3.4$ (2.6) for the co- (counter-) rotation case, respectively, where $1/L_\xi = -(1/\xi)\mathrm{d}\xi/\mathrm{d}\rho$ for any quantity $\xi$. As shown in Fig. 4(b), $1/L_{T_i}$ is almost identical. The values of $1/L_{T_e}$ are shown in Fig. 4(c). As mentioned in Sec. 2.1, the $T_e$ gradient in the co-rotation case is steeper than that in the counter-rotation case in the ITB region. The $n_e$ gradients are virtually identical. Figure 5(a) shows the linear growth rates $\gamma$ and the real frequencies $\omega$ in the low wavenumber region, $0 < k_y\rho_i \leq 1$, for the co- and counter-rotating plasmas at $\rho = 0.45$. At $\rho = 0.45$, the values of $T_e$, $\nu_{*e}$, $\beta_e$, and $\rho_*$ are almost equivalent for the respective cases (Figs. 2(f) and 4(a)), but the $T_e$ gradients differ from each other (Fig. 4(c)). The peaks of $\gamma$ appear around $k_y\rho_i \sim 0.6$ for both cases. In the calculations, the poloidal angle $\theta$ extends from $-5\pi$ to $5\pi$. As shown in Fig. 6, $\phi$ is converged around the boundaries. The spectrum of $\omega$ shows that both cases have the ITG/TEM hybrid modes [19, 20]; $\omega$ continuously changes from the electron to the ion diamagnetic direction with an increase in the wavenumber. This study focuses on the low wavenumber region, $0 < k_y\rho_i \leq 1$, assuming that turbulence is dominated by the region for our cases. We find that in the high wavenumber region, $k_y\rho_i > 1$, $\gamma$ is higher than in the low wavenumber region, but the usual mixing length estimate shows a much smaller $\chi \sim \gamma/k_y^2$ in the high wavenumber region than in the low wavenumber region. Figures 5(b)-5(e) show the radial profiles of $\gamma$ and $\omega$ at $k_y\rho_i = 0.2$, around which the heat flux is maximum, and at $k_y\rho_i = 0.6$, around which the linear growth rate is maximum. As shown in Figs. 5(b) and 5(c), at both wavenumbers, $\gamma$ for the two cases are almost equivalent. Figures 5(d) and 5(e) show that the ITG/TEM modes dominate the ITB region except that a kinetic ballooning mode (KBM) is observed at $k_y\rho_i = 0.2$ for $\rho < 0.4$. There

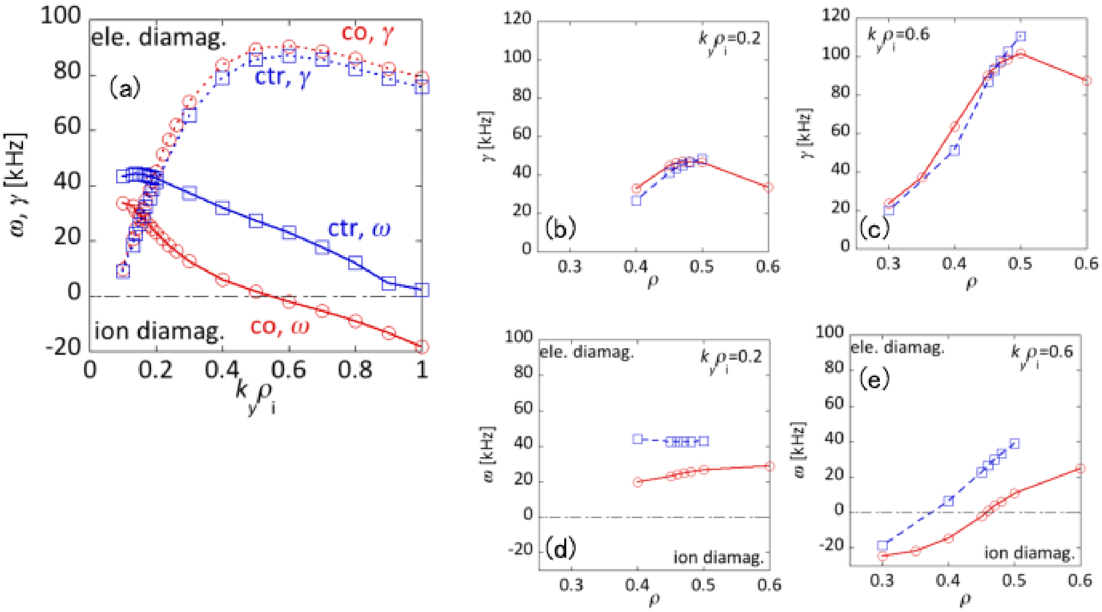


Fig. 5 (a) Comparison of linear growth rates $\gamma$ (dotted lines) and real frequencies $\omega$ (solid lines) at $\rho = 0.45$ for the co-rotating case (circles) and the counter-rotating case (squares) as a function of the poloidal wavenumber $k_y\rho_i$, and radial profiles of $\gamma$ at (b) $k_y\rho_i = 0.2$ and (c) $k_y\rho_i = 0.6$, and $\omega$ at (d) $k_y\rho_i = 0.2$ and (e) $k_y\rho_i = 0.6$ for the co-rotating case (solid lines with circles) and the counter-rotating case (dashed lines with squares).

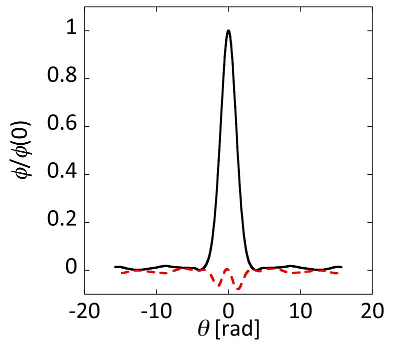


Fig. 6 Normalized electrostatic potential $\phi$ as a function of the poloidal angle $\theta$ at $\rho = 0.45$ and $k_y\rho_i = 0.6$ for the co-rotation case. The real part and imaginary part are denoted by the solid and dashed lines, respectively.

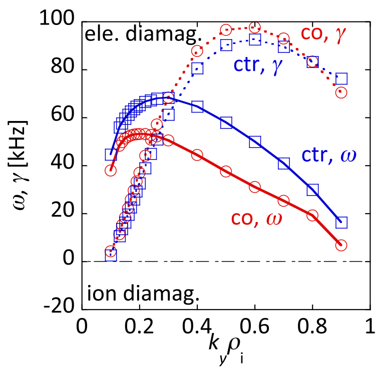


Fig. 7 Comparison of linear growth rate $\gamma$ (dotted lines) and real frequencies $\omega$ (solid lines) at $\rho = 0.45$ for the co-rotating case (circles) and the counter-rotating case (squares) as a function of the poloidal wavenumber $k_y\rho_i$ in the electrostatic limit.

is a difference in $\omega$ of the ITG/TEM modes between the co- and counter-rotation cases: $\omega$ for the counter-rotation case is larger in the electron diamagnetic direction than that for the co-rotation case. This means that the counter-rotation case has a more TEM-like instability than the co-rotation case. The cause of the difference in $\omega$ is described in Sec. 5 and in Appendix. If there is a difference in the dominant mode, the ratio of $\chi_e$ to $\chi_i$ may change [21]. To compare the linear calculations to the experimental values, we estimate $\chi_e^{\mathrm{nonlin}}/\chi_i^{\mathrm{nonlin}}$ by performing the nonlinear calculations. Here, $\chi_i^{\mathrm{nonlin}}$ and $\chi_e^{\mathrm{nonlin}}$ are calculated, using $Q_j = -n_j\chi_j \frac{\mathrm{d}T_j}{\mathrm{d}\rho}\frac{1}{a}$, where the subscript $j$ denotes the particle species. The nonlinear calculations are performed in the electrostatic limit. This may be partly justified by the fact that the dominant instabilities arise by the ITG/TEM turbulence. In addition, as shown in Fig. 7, the linear calculation result in the electrostatic limit shows the similar tendencies to the electromagnetic calculations: $\gamma$ for the two cases is almost equivalent to each other, and the counter-rotation case has the more TEM-like $\omega$ than the co-rotation case. This supports the nonlinear simulations in the electrostatic limit. The comparison of Fig. 5(a) and Fig. 7 also shows that $\gamma$ slightly decreases due to the electromagnetic effect at around $k_y\rho_i = 0.5$.

The insensitivity suggests that the TEM is the dom-

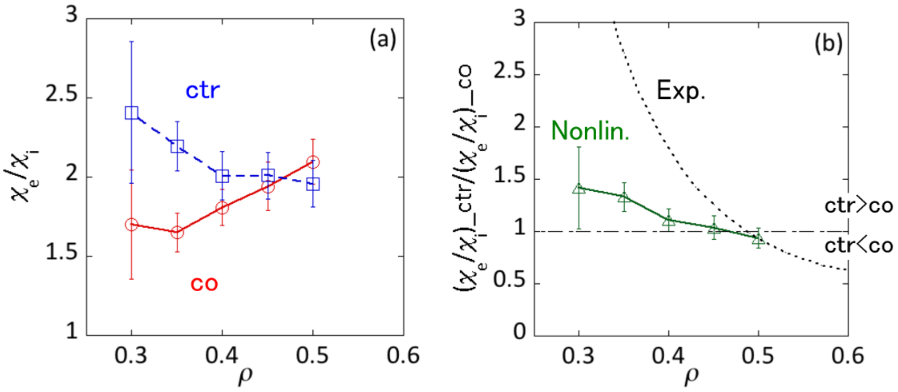


Fig. 8 (a) Comparison of $\chi_e^{\rm nonlin}/\chi_i^{\rm nonlin}$ between the co- (solid line) and counter-rotation (dashed line) cases. (b) Comparison of $(\chi_e/\chi_i)_{\rm ctr}/(\chi_e/\chi_i)_{\rm co}$ between the simulation and the experiment. The solid line is the result from the nonlinear calculations and the dotted line is the experimental result.

inant mode in the linear calculation. On the other hand, $\omega$ becomes larger in the ion diamagnetic direction with the electromagnetic effect. We will investigate the electromagnetic effect on the nonlinear calculations in the future work. The simulation box sizes in the $x$ and $y$ directions are $L_x{\sim}L_y = 62.8\rho_{\rm i}$, respectively, considering the $0 < k_y\rho_{\rm i} \leq 1$ region, where $x$ is the radial direction and $y$ is the binormal direction. The simulation domain along the magnetic field line is $-\pi < \theta < \pi$, but the calculations employ the "twist-and-shift" boundary condition, where the mode at the end of the field line couples the mode at the opposite end of the line [22]. Figure 8(a) shows $\chi_e^{\rm nonlin}/\chi_i^{\rm nonlin}$ calculated by the nonlinear simulations. The error bars denote the standard deviations representing the amounts of variation in $\chi_e^{\rm nonlin}/\chi_i^{\rm nonlin}$ averaged over a certain period of time after the nonlinear saturation. It is confirmed that the TEM dominantly drives the heat transport, as described in Appendix. It is found that $\chi_e^{\rm nonlin}/\chi_i^{\rm nonlin}$ is lower for the co-rotation case than for the counter-rotation case in $\rho \lesssim 0.45$. This result supports the linear calculation result in that there is a difference in the dominant mode; the counter-rotation case has a more TEM-like mode. Next, to compare the difference in $\chi_e^{\rm nonlin}/\chi_i^{\rm nonlin}$ for the two cases with the experimental result, we estimate the ratio of $\chi_e^{\rm nonlin}/\chi_i^{\rm nonlin}$ for the counter-rotation case to that for the co-rotation case, i.e., $(\chi_e^{\rm nonlin}/\chi_i^{\rm nonlin})_{\rm ctr}/(\chi_e^{\rm nonlin}/\chi_i^{\rm nonlin})_{\rm co}$. Figure 8(b) shows the ratio with the experimental one. In this figure, the experimental ratio is estimated as an anomalous value, by subtracting the neoclassical heat diffusivities given by the MI method, as described in Sec. 2.2, from the total heat diffusivities shown in Figs. 2(g) and 2(h). As shown in Fig. 8(b), the ratio calculated by the nonlinear simulations increases towards the magnetic axis. The tendency qualitatively agrees with the experiment. Therefore, it can be concluded that, in the counter-rotation case, the more TEM-like instability with the higher $\chi_e^{\rm nonlin}/\chi_i^{\rm nonlin}$ value than in the co-rotation case results in a degraded $T_{\rm e}$-ITB in the experiment.

In the above investigations, we compares the nonlinear calculation results for the co- and counter-rotation cases by using $\chi_e^{\rm nonlin}/\chi_i^{\rm nonlin}$ instead of the $\chi_j^{\rm nonlin}$ value. This means that we avoid the difficulty in calculating $\chi_j^{\rm nonlin}$ due to the sensitivity of the results and due to analyzing weak magnetic shear plasmas. Actually, we cannot explain the experiments with the nonlinear calculations quantitatively. Comparison between the $\chi_j^{\rm nonlin}$ calculated by the nonlinear simulations and the experimental ones is shown in Fig. 9. The error bars correspond to those for Fig. 8. Figure 9(a) shows the $\chi_i^{\rm nonlin}$ is lower for the counter-rotation case than for the co-rotation case around $\rho = 0.35$. On the other hand, $\chi_e^{\rm nonlin}$ for the two cases is almost equivalent to each other, as shown in Fig. 9(b). These tendencies are not captured in the experiments. We believe that this contradiction may be partly due to the sensitivity of the results to the input values, because the gradients are estimated by the fitted profiles based on the limited number of the discrete measurement points in experiments. Of course there must be some missing physics in our calculations. In addition, this study focuses on the weak magnetic shear region especially for $\rho \lesssim 0.4$. In such regions where the magnetic shear is weak, the radial mode structure tends to expand and the assumptions for the flux-tube simulations to be valid may be potentially violated. Moreover, the fact that in the TEM branch, the electron heat flux tends to be higher than the ion's may lead to $\chi_e^{\rm nonlin} > \chi_i^{\rm nonlin}$ (see e.g., Ref. [23]). For these reasons, to avoid the difficulty in calculating $\chi_j^{\rm nonlin}$, we use $\chi_e^{\rm nonlin}/\chi_i^{\rm nonlin}$ for the comparison of the co- and counter-rotation cases without mentioning the absolute $\chi_j^{\rm nonlin}$ value. Although the nonlinear calculations cannot explain the experiments qualitatively, the difference in $\chi_e^{\rm nonlin}/\chi_i^{\rm nonlin}$ suggests that there is a difference in the dominant mode between the two cases, and agrees with the experiment. Quantitative comparison of $\chi_j$ computed by nonlinear simulations to the experiment's is left for future work.

We also investigate the influence of zonal flows on

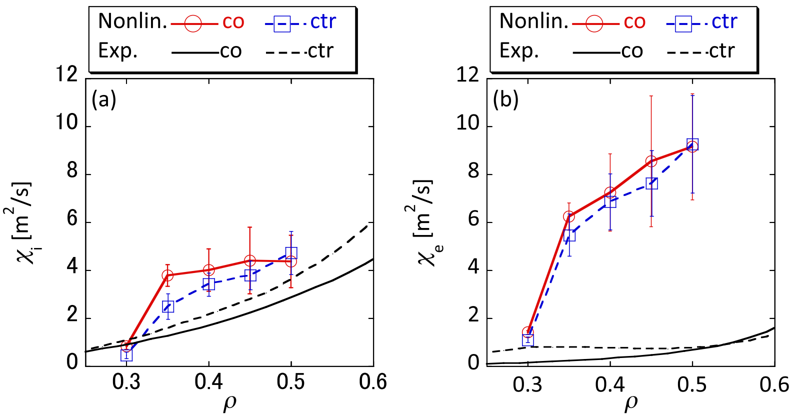


Fig. 9 Comparison of (a) $\chi_i^{\rm nonlin}$ and (b) $\chi_e^{\rm nonlin}$ calculated by the nonlinear simulations with the experimental ones for the co- (solid lines (with circles for the calculation)) and counter- (dashed lines (with squares for the calculation)) rotation cases.

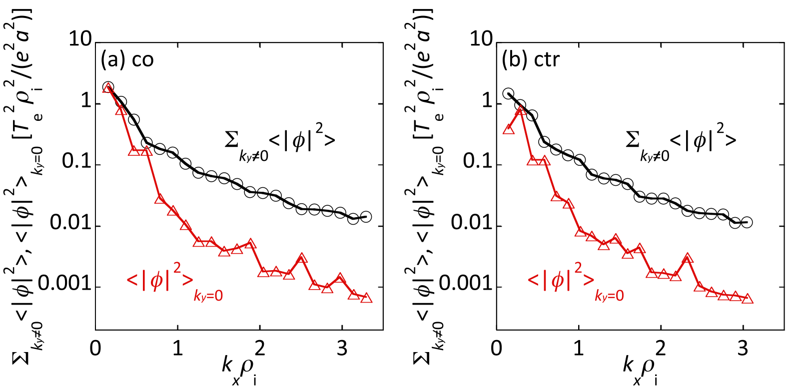


Fig. 10 Squared electrostatic potentials $\langle|\phi|^2\rangle$ averaged over time and the magnetic field line as a function of the radial wavenumber $k_x\rho_i$ for (a) the co-rotation case and (b) the counter-rotation case. The circles and triangles denote $\langle|\phi|^2\rangle$ summed over the poloidal wavenumber $k_y$ except $k_y = 0$ and $\langle|\phi|^2\rangle$ for $k_y = 0$, respectively.

the heat transport. The zonal flow potentials are compared with the turbulent potentials, as shown in Fig. 10. The squared electrostatic potentials $\langle|\phi|^2\rangle$ for $k_y = 0$, $\langle|\phi|^2\rangle_{k_y=0}$, show the zonal flow potentials, and the $k_x\rho_i$ spectra of $\langle|\phi|^2\rangle_{k_y=0}$ are similar for the co- and counter-rotation cases. Here, $\langle|\phi|^2\rangle$ is averaged over a certain period of time after the nonlinear saturation and over the magnetic field line, and is normalized by $e^2a^2/(T_e^2\rho_i^2)$. The turbulent potentials represented by $\langle|\phi|^2\rangle$ summed over $k_y$ except $k_y = 0$, $\sum_{k_y\neq0}\langle|\phi|^2\rangle$, also have similar spectra for the two cases. In accordance with Ref. [24], we estimate the zonal flow amplitude $\sum_{k_x}\langle|\phi|^2\rangle_{k_y=0}$ and the turbulent one $\sum_{k_x,k_y\neq0}\langle|\phi|^2\rangle$, integrating the spectra in Fig. 10. The ratio $\sum_{k_x}\langle|\phi|^2\rangle_{k_y=0}/\sum_{k_x,k_y\neq0}\langle|\phi|^2\rangle$ is 0.553 and 0.326 for the co- and counter-rotation cases, respectively. This means that the influence of the zonal flows is stronger for the co-rotation case than for the counter-rotation case, and therefore that the influence is one of the candidates which explain the improved confinement for the co-rotation case.

## 4. Effects of the Flow Shear

We then investigated the influence of the flow shear on the linear growth rate, with the linear calculations including the flow shear effects. The co- and counter-rotation plasmas have the different toroidal rotation shear due to the difference in their toroidal rotation profiles, as shown in Fig. 2(c). So we investigate how the flow shear influences the linear calculations performed in the previous section. The shear in the direction perpendicular to the magnetic field is the $\boldsymbol{E}\times\boldsymbol{B}$ velocity shear, which reduces turbulent transport. It has been reported that when there is a sufficient $\boldsymbol{E}\times\boldsymbol{B}$ velocity shear, a box type ITB is formed [1, 6]. In addition to the effect of the $\boldsymbol{E}\times\boldsymbol{B}$ velocity shear, the parallel velocity gradient (PVG) of toroidal rotation affects turbulent transport, and this effect is observed in the high flow shear region [10]. These two flow shear effects are implemented in GS2, by solving the following gyrokinetic equation in the frame rotating with the toroidal angular frequency $\Omega$ [10]:

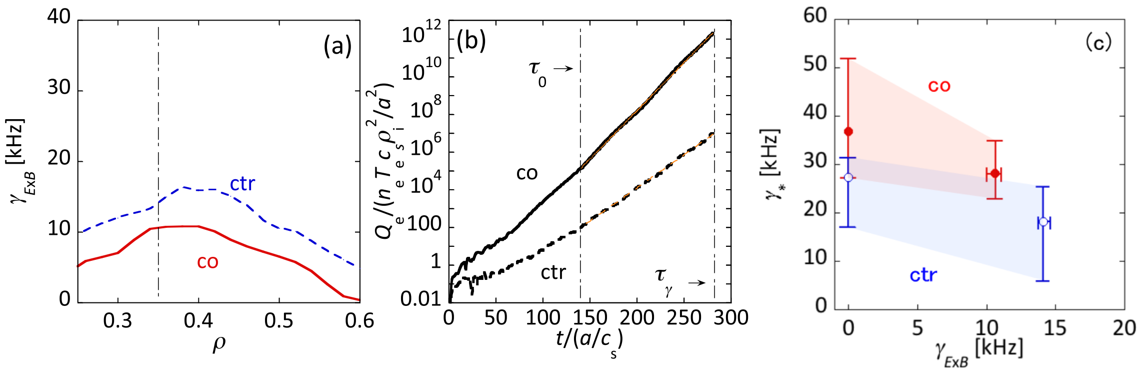


Fig. 11 (a) Radial profiles of the $\boldsymbol{E}\times\boldsymbol{B}$ velocity shear $\gamma_{E\times B}$ for the co-rotating case (solid line) and the counter-rotating case (dashed line). We investigate the flow shear effect at $\rho = 0.35$, as denoted by the vertical chain line. (b) The time evolution of the normalized heat flux $Q_e$ for the co-rotating case (thick solid line) and the counter-rotating case (thick dashed line) with the flow shear effect. The effective linear growth rates $\gamma_*$ are estimated using the fitting lines (thin solid line (co-rotation case) and thin dashed line (counter-rotation case)) and Eq. (4). (c) $\gamma_*$ as a function of $\gamma_{E\times B}$ for the co-rotation case (solid circles) and the counter-rotation case (open circles) at $\rho = 0.35$. At $\gamma_{E\times B} = 0$, the flow shear effects are not included, and at the finite $\gamma_{E\times B}$, the values of which correspond to Fig. 11(a), the flow shear effects are included. The error bars are the maximum and minimum values when the $T_i$, $T_e$ and $n_e$ gradients vary by ±20%.

$$\frac{\mathrm{d}\langle\delta f\rangle}{\mathrm{d}t}+(v_\parallel\hat{\boldsymbol{b}}+\boldsymbol{v}_\mathrm{D}+\langle\boldsymbol{v}_{E\times B}\rangle)\cdot\nabla\left(\langle\delta f\rangle+\frac{e\langle\phi\rangle}{T}F_0\right)$$
$$=\langle C[\delta f]\rangle-\langle\boldsymbol{v}_{E\times B}\rangle\cdot\nabla\psi\left(\frac{\partial F_0}{\partial\psi}+\frac{mv_\parallel}{T}\frac{RB_\mathrm{T}}{B}\frac{\mathrm{d}\Omega}{\mathrm{d}\psi}F_0\right), \quad (1)$$

where $v_\parallel$ is the parallel particle velocity, $\hat{\boldsymbol{b}} = \boldsymbol{B}/B$, $\boldsymbol{v}_\mathrm{D}$ is the drift velocity, $\boldsymbol{v}_{E\times B}$ is the $\boldsymbol{E}\times\boldsymbol{B}$ drift velocity, $F_0$ is a Maxwellian distribution in the frame rotating with toroidal rotation, $C$ is the collision equation, $R$ is the major radius, and $\langle\cdots\rangle$ denotes the average over the gyro angle. The term proportional to $\mathrm{d}\Omega/\mathrm{d}\psi$ on the right hand side of Eq. (1) accounts for the parallel velocity gradient (PVG), which is denoted by $\gamma_\mathrm{p}$, and is related to the equilibrium flow shear $\gamma_\mathrm{E}$ by the geometric factor $(qR/r)$: $\gamma_\mathrm{p} = (qR/r)\gamma_\mathrm{E}$, where $r$ is the half diameter of the flux surface [11]. The definition of $\gamma_\mathrm{E}$ is $\gamma_\mathrm{E} = \frac{\rho}{q}\frac{\partial\Omega}{\partial\rho}$. When a flow velocity is comparable to the sound speed $c_s$, $\Omega$ is given by

$$\Omega(\psi) = -\frac{\mathrm{d}\phi}{\mathrm{d}\psi}, \quad (2)$$

for all species. On the other hand, when the flow velocity is assumed to be much smaller than the sound speed, $\Omega$ is defined as

$$\Omega_j(\psi) = -\frac{\mathrm{d}\phi}{\mathrm{d}\psi}-\frac{1}{n_je_j}\frac{\mathrm{d}p_j}{\mathrm{d}\psi}, \quad (3)$$

in the drift ordering, since the pressure gradient is comparable in magnitude to the electrostatic potential gradient. Preceding work (see e.g., Refs. [12, 13]) typically regards $\Omega$ as in Eq. (2), assuming rapid toroidal rotation. However, in this study we analyze the JT-60U plasmas with the Mach number $M_\mathrm{T}\equiv V_\mathrm{T}/c_s \sim 0.1$. The value of $\Omega$, therefore, should be determined by Eq. (3) based on the drift ordering. On the other hand, the effect of the $\boldsymbol{E}\times\boldsymbol{B}$ velocity shear is incorporated by forcing the radial wavenumbers $k_x$ to depend linearly on time $t$: $k_x(t) = k_{x0} - \gamma_{E\times B}k_yt$, where $k_{x0}$ is the given radial wave number and the definition of $\gamma_{E\times B}$ is the same as that in GLF23, as described in Sec. 2.2 [25]. The radial profiles of $\gamma_{E\times B}$ are described in Fig. 11(a). Linear calculations including the flow shear effects are performed in a simulation box, which is the same as that for the nonlinear calculations in Sec. 3. The "twist-and-shift" boundary condition [22] is also used for the simulation domain along the magnetic field line. The effective linear growth rates $\gamma_*$ obtained with and without the flow shear effects are shown in Fig. 11(c). Here, $\gamma_*$ is defined by the time evolution of the heat flux shown in Fig. 11(b) and the definition is as follows [11, 12]:

$$\gamma_* = \frac{1}{2(\tau_\gamma-\tau_0)}\ln\frac{Q_\mathrm{e}(t=\tau_\gamma)}{Q_\mathrm{e}(t=\tau_0)}, \quad (4)$$

where $Q_e$ is the electron heat flux, and a time evolution from $t = \tau_0$ $(= \tau_\gamma/2)$ to $t = \tau_\gamma$ is used as described in Fig. 11(b). As shown by the solid circles (co-case) and open circles (counter-case) in Fig. 11(c), $\gamma_*$ decreases due to the flow shear effect. We also investigate the sensitivity of $\gamma_*$ to the $T_i$, $T_e$ and $n_e$ gradients, because the calculation results are generally sensitive to the gradients. Considering the experimental errors, which are estimated to be about 10%, the vertical error bars for the case with $\gamma_{E\times B} = 0$ in Fig. 11(c) show the maximum and minimum values of $\gamma_*$ when the $T_i$, $T_e$ and $n_e$ gradients vary by ±20%. In addition, to obtain the vertical and horizontal error bars for the case with the finite $\gamma_{E\times B}$, the $T_i$, $T_e$ and $n_e$ gradients vary by ±20% with the pressure gradient term in the force balance equation: $E_r$ changes due to the pressure gradient, with the fixed toroidal rotation profile. The values of $\gamma_*$ decrease due to $\gamma_{E\times B}$ in the range of the vertical error bars. We thus do not find the evidence that the flow shear has significant effect on the linear growth rates shown in Fig. 5. However, in these calculations, since the radial wavenumbers depend on time, the real frequency is not given, as that is given in the linear calculations. The flow shear effect on the TEM, therefore, cannot be revealed. We will investigate the effect in the near future.

## 5. Conclusions and Discussion

To clarify the relationship between the direction of toroidal rotation and heat transport in the ITB region, we first simulate heat transport using the GLF23 model. As a consequence, GLF23 does not predict the difference in turbulent transport between the co- and counter-rotation cases. Next the linear calculations using the flux-tube gyrokinetic code GS2 show that the values of $\gamma$ of the co- and counter- rotating plasmas are comparable in magnitude. However, there is a difference in the value of $\omega$ between the two cases, and the counter-rotating plasma has the more TEM-like instability. In addition, the nonlinear calculations show that $\chi_e/\chi_i$ is higher for the counter-rotation case than for the co-rotation case. A similar tendency is observed in the experiment. It can, therefore, be concluded that the difference in the dominant mode is related to the change in the gradient of the $T_e$-ITB in the experiment. The linear calculations including the flow shear effect show that the effect reduces $\gamma_*$ for both cases. However, since the reduction in $\gamma_*$ is less than the change in $\gamma_*$, according to the sensitivity study that considers the experimental errors, the flow shear effect on the linear growth rate is not significant. This study includes both the $\boldsymbol{E} \times \boldsymbol{B}$ velocity gradient and the PVG in the flow shear effect. To clarify the two effects individually, we will perform these calculation cases in the future, artificially setting them to include only one of the effects. In addition, the value of $\gamma_{E\times B}$ sufficient to fully suppress $\gamma_*$ will be estimated so as to explore plasmas with improved energy confinement.

The candidates causing the difference in $\omega$ by the linear calculations are the $T_e$ gradient and $Z_{\mathrm{eff}}$, both of which have different values between the co- and counter-rotation cases. We now study the dependence of linear calculations on the $T_e$ gradient and $Z_{\mathrm{eff}}$. As a result, it is found that $\omega$ is influenced by $Z_{\mathrm{eff}}$ rather than the $T_e$ gradient, and tends to be more TEM-like as $Z_{\mathrm{eff}}$ increases. It is also confirmed that $\chi_e^{\mathrm{nonlin}}$ increases with $Z_{\mathrm{eff}}$. These results imply that the fact that $Z_{\mathrm{eff}}$ is lower for the co-rotation case than that for the counter-rotation case is one of the potent candidates to explain the experimental result. We experimentally know that counter-rotating plasmas tend to have higher $Z_{\mathrm{eff}}$ values than co-rotating ones in JT-60U. The influence of $Z_{\mathrm{eff}}$ on heat transport will be investigated quantitatively in future work. In addition to the $T_e$ gradient and $Z_{\mathrm{eff}}$, the flow shear also depends upon a rotation profile. When we consider the change in the flow shear, it is found that for our cases counter rotation acts as the stabilization. Therefore the change in the flow shear may not be the key to explain the improved confinement for the co-rotation case. These parametric dependences are described in detail in Appendix.

GLF23 does not predict that the TEM is the dominant mode. This may be the reason why GLF23 fails to reproduce the difference in the $T_e$-ITB between the co- and counter-rotation cases, when it is concluded that the TEM is related to the gradient of the $T_e$-ITB. The more advanced transport model TGLF [26, 27] more comprehensively employs the physics of trapped particles than GLF23. We will therefore check whether TGLF predicts the more TEM-like instability for the counter-rotation case than for the co-rotation case, as shown by the GS2 linear calculations. If the characteristic of $\omega$ is predicted, the difference in the $T_e$-ITB will be reproduced in the transport simulation.

This paper investigates two plasmas to study the relationship between toroidal rotation and heat transport. To further confirm the results obtained with the two plasmas, we will analyze the other plasma subsets, in which the direction of toroidal rotation changes. In the additional analyses, for a quantitative comparison between the experimental and calculation results, the plasmas which are measured in detail especially $Z_{\mathrm{eff}}$ have to be chosen. The qualitative comparison will also require the finite-$\beta$ effect, which is neglected in the nonlinear simulations in this paper, because we find that the linear calculation results are influenced by the finite-$\beta$ effect. In addition, we also regard the relationship between the particle flux and the toroidal rotation direction as an interesting subject.

## Acknowledgments

The authors would like to thank Dr. M. Nakata for helpful discussions on the gyrokinetic code. They are also grateful to Dr. R.V. Bravenec for his helpful comments on the GS2 code. One of the authors (E.N.) thanks Drs. Y. Kamada, T. Fujita, N. Oyama, M. Yoshida, and T. Takizuka for their fruitful discussions and continuous encouragement during her stay in JAEA as a fellow of advanced science. This work was carried out using the HELIOS supercomputer system at International Fusion Energy Research Centre, Aomori, Japan, under the Broader Approach collaboration between Euratom and Japan, implemented by Fusion for Energy and JAEA. This work was supported by Research Fellowships of Japan Society for the Promotion of Science for Young Scientists.

## Appendix. Parametric Dependences of Linear and Nonlinear Calculation Results

To study the key parameter to the change in the $T_e$-ITB with the rotation direction, we investigate the dependences of the calculation results on the grad $T_e$, $Z_{\mathrm{eff}}$ and the flow shear.

The difference in the $T_e$ gradient between the co- and counter-rotation cases is shown in Fig. 4(c). As a result of studying the influence of the difference in the $T_e$ gradient on the linear and nonlinear calculations, it is found that while $\gamma$ clearly increases as the gradient increases, $\chi_e^{\rm nonlin}$ changes slightly with the gradient. Therefore, the $T_e$ gradient does not significantly alter turbulent transport, and may not be the cause of the improved confinement for the co-rotation case. In addition, it is found that since $\chi_e^{\rm nonlin}$ is not sensitive to the $T_e$ gradient, for our cases the experimental error in the $T_e$ gradient is not the cause of the difficulty in comparing the experimental and simulation results. Moreover, we can indicate the dominant mode with the $T_e$ gradient scan. Figure A1 shows the comparison between the $k_y\rho_i$ spectra of $\langle|\phi|^2\rangle$ for the nominal co-rotation case and for the case where the normalized electron temperature gradient $1/L_{T_e}$ which mainly drives the TEM is set to zero. Here, the other parameters remain unchanged for the nominal co-rotation case. As shown in this figure, $\langle|\phi|^2\rangle$ becomes higher by almost an order of magnitude due to the TEM. The counter-rotation case also show the similar tendency. This means that the TEM dominantly causes the heat transport in the nonlinear calculations. We note that the influence of the TEM is not completely eliminated in the case with $1/L_{T_e} = 0$, because the case includes the effects of the impurities which can affect the TEM.

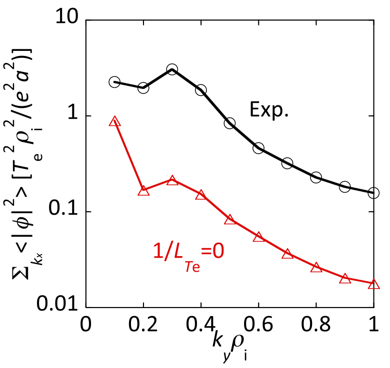


Fig. A1 Squared electrostatic potentials $\langle|\phi|^2\rangle$ averaged over time and the magnetic field line as a function of the poloidal wavenumber $k_y\rho_i$ for the co-rotation case. The circles and triangles denote the cases with the nominal values for the experiments and with the electron temperature gradient $1/L_{T_e} = 0$, respectively.

Next, the influence of $Z_{\rm eff}$ on the linear and nonlinear calculations is studied. Here, the ratio of the main ion density to the impurity density varies with $Z_{\rm eff}$. Figure A2(a) shows the change in $\gamma$ and $\omega$ by the electromagnetic linear calculations for the counter-rotation case at $\rho = 0.45$. $Z_{\rm eff}$ varies from 1.0 to 3.5, which is the nominal value for the counter-rotation case. It is found that varying $Z_{\rm eff}$ greatly influences $\omega$ and moderately, $\gamma$. As shown in Fig. A2(b), nonlinear simulations reveal that $\chi_e^{\rm nonlin}$ normalized by the gyro-Bohm unit $\rho_i^2 c_s/a$, which is estimated based on the counter-rotation case, does decrease when $Z_{\rm eff}$ varies from 3.5 (nominal, counter case) to 3.0 (nominal, co case) for the counter-rotation case at $\rho = 0.35$. These results imply that the fact that $Z_{\rm eff}$ is lower for the co-rotation case than that for the counter-rotation case is one of the potent candidates to explain the experimental result in that $\chi_e$ is lower for the co-rotation case than for the counter-rotation case. It is also suggested that the experimental error in $Z_{\rm eff}$ may influence the analyses of experiments due to the sensitivity of $\chi_e^{\rm nonlin}$ to $Z_{\rm eff}$.

Finally, we study the influence of the flow shear, which depends upon a rotation profile. $E_r$ would be always negative due to the diamagnetic effect if rotation were not taken into account. Through the radial force balance, counter-toroidal rotation enhances the negative $E_r$ and its radial gradient is typically steeper for the counter-rotation plasma than for the co-rotation plasma, because co-toroidal rotation tends to weaken the negative $E_r$ and sometimes produces the positive $E_r$, depending on the rotation speed. In this way, the flow shear changes with the rotation direction. We now investigate the effect of the flow shear on the effective linear growth rate $\gamma_*$, based

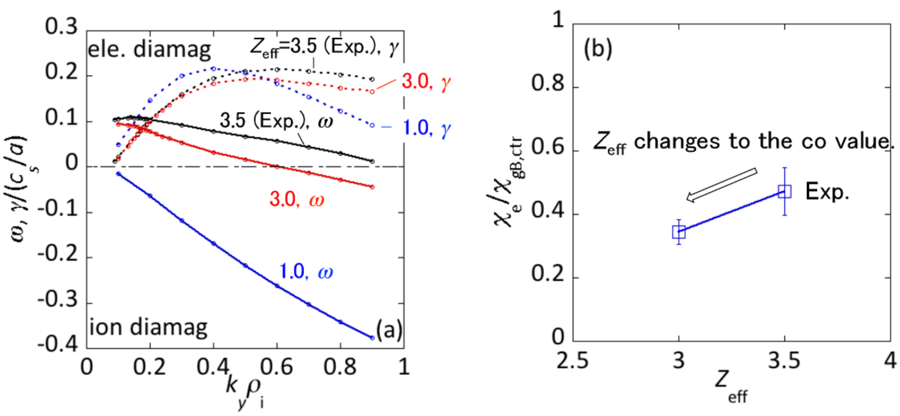


Fig. A2 The $Z_{\rm eff}$ scan. (a) Linear growth rates $\gamma$ (dotted lines) and real frequencies $\omega$ (solid lines) versus wavenumber for the counter-rotation case at $\rho = 0.45$: $Z_{\rm eff}$ varies from 1.0 to 3.5. (b) $\chi_e^{\rm nonlin}$ versus $Z_{\rm eff}$ for the counter-rotation case at $\rho = 0.35$: $Z_{\rm eff}$ varies from 3.5 (nominal, counter case) to 3.0 (nominal, co case).

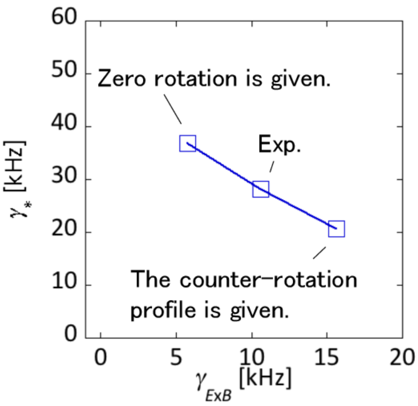


Fig. A3 The $\gamma_{E\times B}$ scan. The effective linear growth rate $\gamma_*$ versus the $E\times B$ velocity shear $\gamma_{E\times B}$ for the co-rotation case at $\rho = 0.35$ in the three cases: the nominal co-rotation case ($\gamma_{E\times B} = 10.6$), the zero-rotation case over the entire profile ($\gamma_{E\times B} = 5.8$) and the case where a rotation profile is replaced by that for the counter-rotation case ($\gamma_{E\times B} = 15.6$).

on the parameters for the co-rotation case at $\rho = 0.35$. In the flow shear scan, we prepare for three cases: the nominal co-rotation case, the zero-rotation case over the entire profile and the case where a rotation profile is replaced by that for the counter-rotation case. With this assumption, the $\boldsymbol{E} \times \boldsymbol{B}$ velocity shear, $\gamma_{E\times B}$, changes from 10.6 (nominal) to 15.6 (nominal to counter) and to 5.8 (nominal to zero). The other parameters remain unchanged for the co-rotation case. Figure A3 shows the linear growth rates as a function of $\gamma_{E\times B}$, clearly indicating that $\gamma_*$ decreases as $\gamma_{E\times B}$ increases due to the $\boldsymbol{E} \times \boldsymbol{B}$ flow shear stabilization. Within this range, the effect of destabilization by the parallel velocity gradient is less than that of stabilization by the $\boldsymbol{E} \times \boldsymbol{B}$ flow shear. This result implies that from the aspect of the flow shear, counter rotation acts as the stabilization through the steeping of the $E_r$ gradient, and that the change in the flow shear due to the change in the rotation direction may not be the key to explain the improved confinement for the co-rotation case.


[1] H. Shirai *et al.*, Nucl. Fusion **39**, 1713 (1999).
[2] N. Oyama *et al.*, Nucl. Fusion **47**, 689 (2007).
[3] Y. Kamada *et al.*, Nucl. Fusion **51**, 073011 (2011).
[4] B.J. Green for the ITER International Team and Participant Teams, Plasma Phys. Control. Fusion **45**, 687 (2003).
[5] T. Fujita, Plasma Phys. Control. Fusion **44**, A19 (2002).
[6] G. Rewoldt *et al.*, Nucl. Fusion **42**, 403 (2002).
[7] H. Urano *et al.*, Nucl. Fusion **48**, 085007 (2008).
[8] M. Kotschenreuther *et al.*, Comput. Phys. Commun. **88**, 128 (1995).
[9] W. Dorland *et al.*, Phys. Rev. Lett. **85**, 5579 (2000).
[10] M. Barnes *et al.*, Phys. Rev. Lett. **106**, 175004 (2011).
[11] C.M. Roach *et al.*, Plasma Phys. Control. Fusion **51**, 124020 (2009).
[12] E.G. Highcock *et al.*, Phys. Plasmas **18**, 102304 (2011).
[13] W. Guttenfelder and J. Candy, Phys. Plasmas **18**, 022506 (2011).
[14] R.E. Waltz *et al.*, Phys. Plasmas **4**, 2482 (1997).
[15] J.E. Kinsey *et al.*, Phys. Plasmas **12**, 052503 (2005).
[16] N. Hayashi and JT-60 Team, Phys. Plasmas **17**, 056112 (2010).
[17] M. Honda *et al.*, Nucl. Fusion **53**, 073050 (2013).
[18] M. Kikuchi and M. Azumi, Plasma Phys. Control. Fusion **37**, 1215 (1995).
[19] J.A. Baumgaertel *et al.*, Phys. Plasmas **19**, 122306 (2012).
[20] R.V. Bravenec *et al.*, Phys. Plasmas **20**, 104506 (2013).
[21] E. Narita *et al.*, Plasma Fusion Res. **8**, 1403082 (2013).
[22] M.A. Beer *et al.*, Phys. Plasmas **2**, 2687 (1995).
[23] J. Candy, Phys. Plasmas **12**, 072307 (2005).
[24] M. Nunami *et al.*, Phys. Plasmas **19**, 042504 (2012).
[25] G.W. Hammett *et al.*, Bull. Am. Phys. Soc. (2006), Abstract No.VP1.136.
See http://meetings.aps.org/link/BAPS.2006.DPP.VP1.136
[26] G.M. Staebler *et al.*, Phys. Plasmas **14**, 055909 (2007).
[27] J.E. Kinsey *et al.*, Phys. Plasmas **15**, 055908 (2008).